Technical Report 1647
April 1994

Surface Ship Infrared Signature Model Evaluation

C. P. McGrath
D. R. Jensen
P. P. Ostrowski

EXECUTIVE SUMMARY

OBJECTIVE

This paper compares measured infrared data of the Research Vessel *Point Sur* (R/V *Pt. Sur*) with predictions from two ship temperature prediction codes. The prediction codes are the Ship Signature (SHIPSIG) model developed by Naval Surface Weapons Center, and the TCM2 model developed by Georgia Technical Research Institute (GTRI). TCM2 is the target model used in the Electro-Optical Tactical Decision Aid (EOTDA) that is being integrated into the Tactical Environmental Support System (TESS) and Tactical Aircraft Mission Planning System (TAMPS). SHIPSIG is a simplified computer model that is used for comparison.

RESULTS

The R/V *Point Sur* was instrumented with surface-mounted thermistors and meteorological measurement equipment. Thermal images were collected with an airborne AGA-780 imaging radiometer installed in a Piper *Navajo* aircraft. The integrated ship temperature from each thermal image was adjusted to a zero-range value using the LOWTRAN 6 atmospheric prediction code to determine the path radiance and transmission effects. Attempts to relate the image temperatures to thermistor values showed inconsistent correlation, so only the AGA-780 image temperatures are presented here. The measurement uncertainty of the airborne AGA-780 system is less than two degrees Celsius. Both SHIPSIG and TCM2 compared favorably (within two degrees Celsius) with the measured values, regardless of viewing angle. The only exception occurred at sunset, where TCM2 over-predicted the ship temperature by four degrees.

RECOMMENDATIONS

Both SHIPSIG and TCM2 produced good results with this limited data set. This test case was for a clear weather day. Further study should validate the model under more diverse weather conditions. The data indicate TCM2 may be over-predicting solar loading when the sun is low in the sky; however, this could simply be an anomaly of this data set. Further investigation should be performed with empirical data that are more accurate, such as from the AGEMA 900 imaging system (calibrated to within one-half degree) recently purchased by NRaD.

CONTENTS

FIGURES

INTRODUCTION

BACKGROUND

The Ocean and Atmospheric Sciences Division, Code 54, of the Naval Command, Control and Ocean Surveillance Center RDT&E Division (NRaD) has developed computer codes for assessing the performance of airborne passive infrared surveillance systems operating against surface ships. One such code, the prediction of Performance and Range of Electro-Optical Systems (PREOS) presently resides in the U.S. Navy's Tactical Environmental Support System (TESS). The present version of PREOS addresses the ability of airborne Forward-Looking Infrared (FLIR) systems to perform range-dependent tasks, such as detection, classification, and identification of surface targets. The range at which a sensor can effectively perform depends upon the target's infrared radiance contrast with the naturally occurring background and the transmittance of the intervening atmosphere. The atmospheric transmittance diminishes the radiance contrast with range due to the effects of molecular absorption by the gaseous constituents and the absorption and scattering of suspended particulates (aerosols) and hydrometers (rain and snow). For a simple detection task, the maximum performance range is that range at which the target-background contrast is reduced by the transmittance to the minimum difference detectable by the sensor. The PREOS algorithm is presently based on a fixed temperature difference between a rectangular target and the sea background. This approach neglects (1) the effects of a wind-ruffled sea on the sky reflections, (2) emissions from the surface, and (3) the intervening atmospheric contributions to the total background radiance scene, which changes with viewing angle and altitude of the sensor. Also, without knowing the ship's actual temperature, which is dependent on its history (course, speed, and surrounding meteorological parameters), it is questionable that the detection range to an adversary target can ever be predicted with any assured degree of accuracy.

The PREOS code was recently updated (McGrath, 1992) to allow a ship commander, when aware of his ship's past and future courses, to use the prediction algorithm to determine the ranges at which an adversary can detect and track the ship using passive infrared sensors. These standoff ranges are of primary importance to estimate the times allowable for either evasive action against guided weaponry launched at the ship or for the deployment of countermeasures. For this application, the Ship Signature (SHIPSIG) computer code (Ostrowski & Wilson, 1985) developed at the Naval Surface Warfare Center is used to determine the ship's temperature history. SHIPSIG approximates the complex structure of a ship with plane vertical and horizontal elements that represent the ship's temperature at zero-range on an average basis. In the present model, the rectangular elements and ship stack correction factors apply to four large combatants (Ostrowski, 1993) and the R/V *Point Sur.* (The R/V *Point Sur* is a 135-ft research ship, owned by the National Science Foundation, that is operated for a consortium of Central California educational institutions, including the Naval Postgraduate School, Monterey, California.) The model requires as inputs: the ship's course and speed, as a function of time from a starting geographic latitude; the surface wind speed and direction; visibility; relative humidity; air temperature; the ship's initial temperature; cloud cover; and the viewing angle. The primary computational vehicle used in the updated PREOS, for calculating the aforementioned contributors to the sea background radiance, is a modified version (Wollenweber, 1988 & 1990) of the U.S. Air Force Atmospheric transmittance/radiance Code LOWTRAN 6 (Kneizys et al., 1983) that uses measured profiles of meteorological parameters as inputs. In this code, the sea surface

wave slopes are assumed to be Gaussian, distributed with variances in the upwind and cross-wind directions that are directly proportional to wind speed (Cox & Monk, 1954).

Solar glint, cloud emissions, and shadows contributing to the apparent radiance of the sea are not addressed in the PREOS radiance algorithm. PREOS will be replaced by the Mark III version of the U.S. Air Force Electro-Optical Tactical Decision Aid (EOTDA) (Freni et al., 1993), which will be incorporated into version 3.0 of TESS in FY 94. The Mark III EOTDA currently provides many sensor types and thermal models of several targets, including two ships (a frigate and a gunboat), and a variety of backgrounds. (The gunboat model is based on the characteristics of the R/V *Point Sur.*) The propagation environment is modeled as a simple two-layer atmosphere with explicit cloud contribution to down-welling radiance, but assumes a cloud free, line-of-sight from the target to the sensor. The thermal model used to compute target temperatures, Target Contrast Model #2 (TCM2) (Blackeslee & Rodriguez, 1992), treats the target as a distinctive three-dimensional network of nodes that exchange heat with one another and their environment.

TCM2 applies first-principles physics to the thermal interactions among interconnected three-dimensional nodes in a given atmosphere. SHIPSIG considers the target as a rectangular surface that interacts over time with the atmosphere. The TCM2 approach has the advantage of more accurately producing the target image. It also indicates hot and cold spots within the target area, which is useful at close ranges. Both SHIPSIG and TCM2 continuously track changes of ship's temperatures as headings change; however, as TCM2 is implemented in EOTDA, a constant ship's heading is assumed. Both models require knowing meteorological and navigational conditions several hours prior to the time of interest, so that the models can stabilize at a steady starting point. When this is not feasible, SHIPSIG uses ambient temperature as the starting target temperature, and TCM2 performs an integration, back in time from the known conditions, to initialize the model.

To date, the ship temperature models in the EOTDA and PREOS have not received adequate validation. It is the purpose of this report to utilize a set of airborne thermal images of the R/V *Point Sur* (obtained simultaneously with measurements of meteorological parameters) to calculate the zero-range, average ship temperatures for comparison with those predicted by the differing ship models.

MEASUREMENTS

During July and August 1992, NRaD (Code 543) performed airborne temperature measurements of the R/V *Point Sur* off the coast of northern California using a calibrated 8- to 12-μm thermal imaging system. The system was mounted in a Piper *Navajo* aircraft that was flown at low altitudes within the proximity of the ship. Stratus clouds were present throughout most of the cruise; however, the cloud cover abated after about 2000 Greenwich Mean Time (G.M.T.) on 3 August, and clear skies prevailed on 4 August. For this case study, these cloud-free portions of the data set have been selected for the ship temperature model comparisons.

Vertical profiles of meteorological parameters were obtained using a VAISALA, Model RS80, radiosonde system onboard the R/V *Point Sur.* When calibrated, the VAISALA measures pressure (±0.5 mb), temperature (±0.2 °C), and relative humidity (±2%) as a function of altitude. The Naval Postgraduate School provided the meteorological data derived from the balloon launches onboard the R/V *Point Sur.* The times of these data sets coincided close to those of the radiance measurements. An NRaD computer code was used to convert the data to digitized profiles compatible for implementation to LOWTRAN.

Sea temperatures, surface wind data, and radon concentrations were also recorded onboard the R/V *Point Sur* throughout the measurement period. The radon concentration values were used to determine the type (continental or marine) of air mass present. Global Position Satellite (GPS) receivers were operated onboard the aircraft and the ship throughout the measurement period to obtain navigational data. This GPS reckoning of the two platforms, together with the aircraft altitude, allowed the viewing angle and slant range of the ship from the aircraft to be calculated. Although the ship maneuvered periodically on each day, its general heading, as a function of time after departing Monterey, California on 29 July, is shown in figure 1 for the period ending on 4 August 1992.

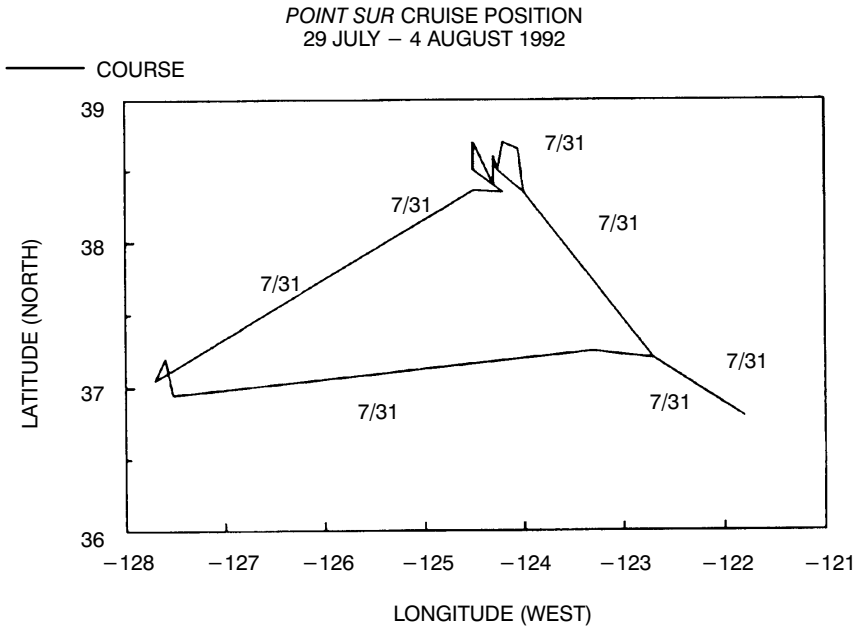

Figure 1. Position of the R/V *Point Sur* as a function of time after departing Monterey, California on 29 July 1992.

The thermal imaging system (AGEMA Model 780) had a 2.95-degree Field-Of-View (FOV) lens. The response of the system was determined by placing a blackbody of known temperature (±0.1 °C, for temperatures <50 °C) in front of the lens at the minimum focusing distance of 300 cm. The digitized video signal transfer function of the system then allowed the blackbody temperature to be reproduced to within ±0.2 °C. The data processing software (CATS 2.00) of the AGEMA system allows the digitized image of the thermal scene to be displayed on a computer terminal. The resolved scene is represented across 128 pixels at 0.023 °C per pixel. The effective blackbody temperature corresponding to each pixel can be displayed by positioning a cursor at the appropriate position. The CATS software also allows the pixels, whose temperatures are either above or below a certain level, to be deleted from the thermal image. A temperature histogram of the remaining pixels, in a selected area of the image, can then be displayed. With this process, the average ship's temperature can be determined because the pixels that remain pertain to the radiance of the ship itself (independent of background).

CALCULATIONS OF ZERO-RANGE AVERAGE SHIP'S TEMPERATURES

The average radiance measured by the AGEMA, $N(R)_{meas}$, at a range R, is the sum of the effective blackbody average radiance of the ship at zero-range, $N(R = 0)_{ship}$, and the atmospheric emission along the path $N(R)_{path}$; for example,

$$N(R)_{meas} = N(R = 0)_{ship}\, \tau(R) + N(R)_{path}\,, \tag{1}$$

where $\tau(R)$ is the atmospheric transmittance at the range R. $N(R)_{meas}$ is obtained by converting the average temperature measured by the AGEMA to radiance using Planck's function integrated over the 8- to 12-μm wavelength band. The atmospheric transmittance and radiance over the slant path is determined from a modified LOWTRAN 6 code employing the U.S. Navy Aerosol Model (NAM), as it appears in LOWTRAN 7 (Kneizys et al., 1988). The slant path is defined by the aircraft's altitude and the zenith angle of the target. Applying these values to Equation (1) solves for $N(R = 0)_{ship}$. Then $N(R = 0)_{ship}$ must be converted to the average temperature of the ship at zero-range, $T(ship)$, using Planck's function.

To calculate the path transmittances and radiances, the LOWTRAN code requires the vertical profiles of pressure, temperature, and relative humidity. When operated with the Navy Aerosol Model (NAM), the current wind speed, the 24-hour averaged wind speeds, and the origin of the air mass are also required as inputs. If surface visibility is known, the LOWTRAN code allows it to be input, and it scales the aerosol model such that the visibility calculated at a wavelength of 0.55 μm (using Koschmieder's equation) is the same as the observed value. If the visibility is not available, the code calculates a visibility from the unscaled distribution. Surface visibility was not recorded onboard the R/V *Point Sur*, so the calculated visibilities were used in the model evaluations.

The origin of the air mass was determined by the air mass factor (referred to as ICSTL in LOWTRAN 6) appearing in the first component of NAM. In the original version of LOWTRAN 6, ICSTL is related to the concentration of atmospheric radon, Rn, by the relation

$$ICSTL = INT(Rn/4) + 1\,, \tag{2}$$

where *Rn* is the measured radon content expressed in pCi/m^3, and INT refers to the closest integer value of (*Rn*/4). In the original version of LOWTRAN 6, ICSTL is allowed to range between integer values of one, for open ocean conditions, and ten, for coastal regions. For the data set used here, measurements of radioactive radon were made onboard the R/V *Point Sur* using an Automatic Radon Counter (ARC-2A) (Littfin, 1992). The measured values of *Rn* caused the ICSTL index to exceed the previously defined upper limit of ten. This prompted an additional modification to LOWTRAN 6, to allow the use of non-integer values exceeding ten.

Examples of the path transmittances and radiances, calculated at the times of the AGEMA measurements on 4 August, are shown in figure 2. The variations with time between these two parameters are as to be expected; for example, an increase or decrease in transmittance results in a decrease or increase, respectively, in path radiance. It had been anticipated that temperature measurements using thermistors and a hand-held radiometer onboard the R/V *Point Sur* would allow the calculations to be validated; however, it was found that the "ground-truth" measurements by the different instruments at the same locations differed as much as one degree Celsius, and that these exact locations on the ship could not be identified on the AGEMA thermogram.

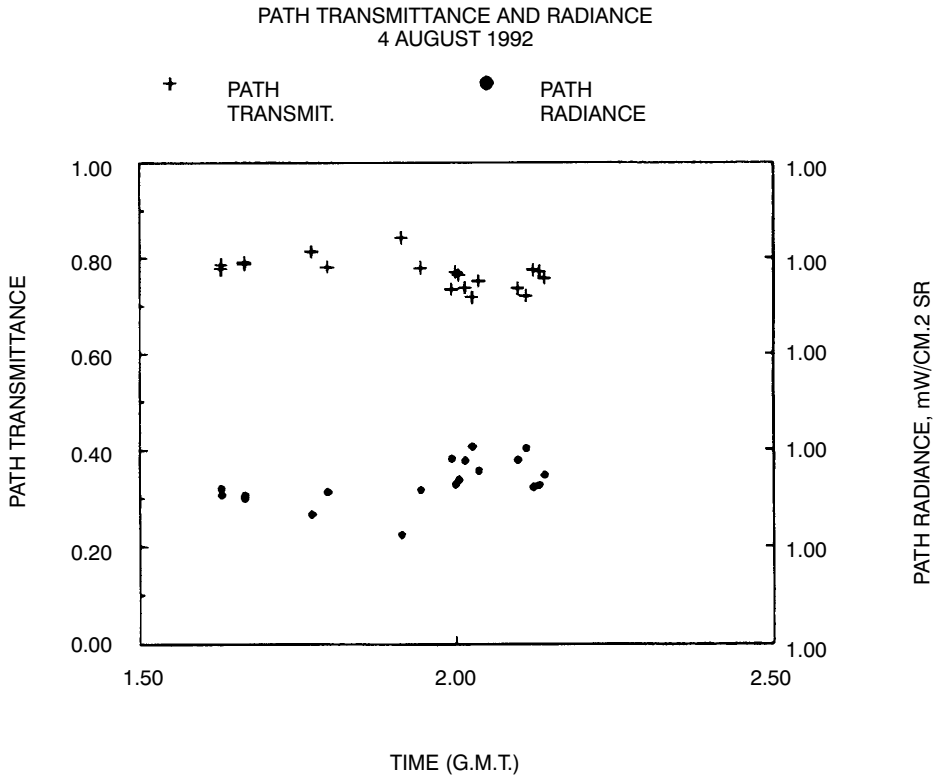

Figure 2. Calculated path radiances and transmittance as a function of time on 4 August 1992.

In figure 3, the upper plot shows the average ship's temperature as a function of time, for the port and starboard sides of the R/V *Point Sur,* as measured 4 August by the airborne AGEMA. The lower plot in figure 3 shows the same temperature values corrected for atmospheric effects. The corrected ship temperatures for all of the days (including the meteorological parameters, path transmittances, and radiances used in these calculations) have been reported in an earlier report (Hughes & McGrath, 1993).

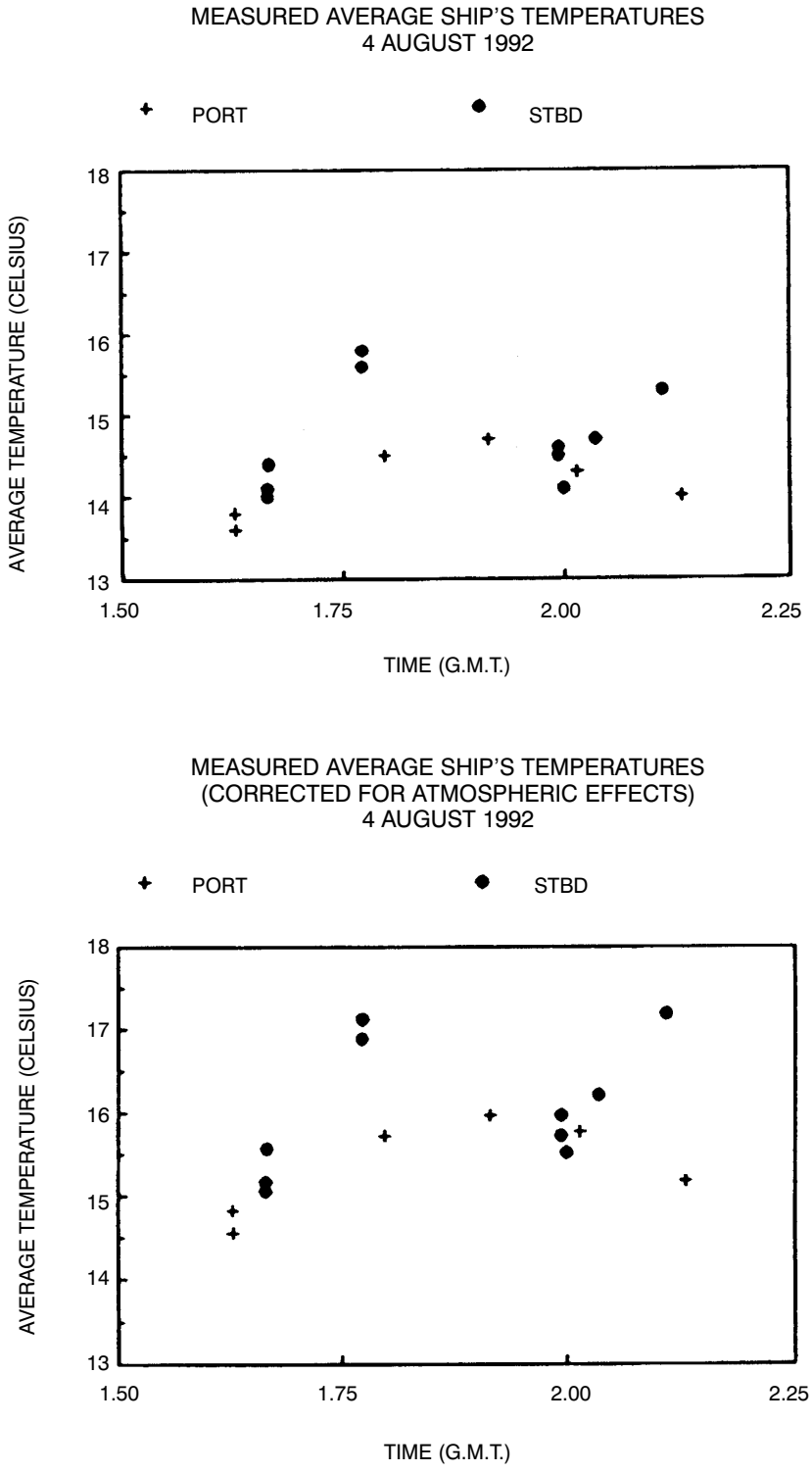

Figure 3. Average temperatures, as measured by the AGEMA onboard the aircraft (upper) and their values corrected for atmospheric effects (lower) as a function of time for the port and starboard sides of the R/V *Point Sur* on 4 August 1992.

COMPARISON OF MEASURED AND MODELED AVERAGE SHIP'S TEMPERATURES

The heading of the R/V *Point Sur*, with respect to the sun's azimuth and zenith angle, is illustrated in figure 4. On 3 August, the ship's heading was easterly (82 degrees true north) with the sun positioned off the starboard bow at 1900 hours G.M.T. Near 2000 hours, ship's heading was changed to 324 degrees, true north, placing the port quarter toward the sun. The ship remained on this heading for approximately one hour before returning to an easterly course (101 degrees, true north) at close to 2200 hours. Later, at 0030 hours (G.M.T) on 4 August (labeled as 24.5 hours, figure 4) the ship again changed course to a northwesterly heading (325 degrees, true north) placing the sun off the port bow. The ship remained on this heading for approximately 30 minutes before returning to an easterly course (111 degrees, true north), which placed the sun off the starboard quarter. Previously, during the first course heading on 3 August, the sun was high in the sky (zenith angle ≈ 20 degrees) as compared to its position during the second course change where the sun (zenith angle ≈ 88 degrees) was close to the horizon.

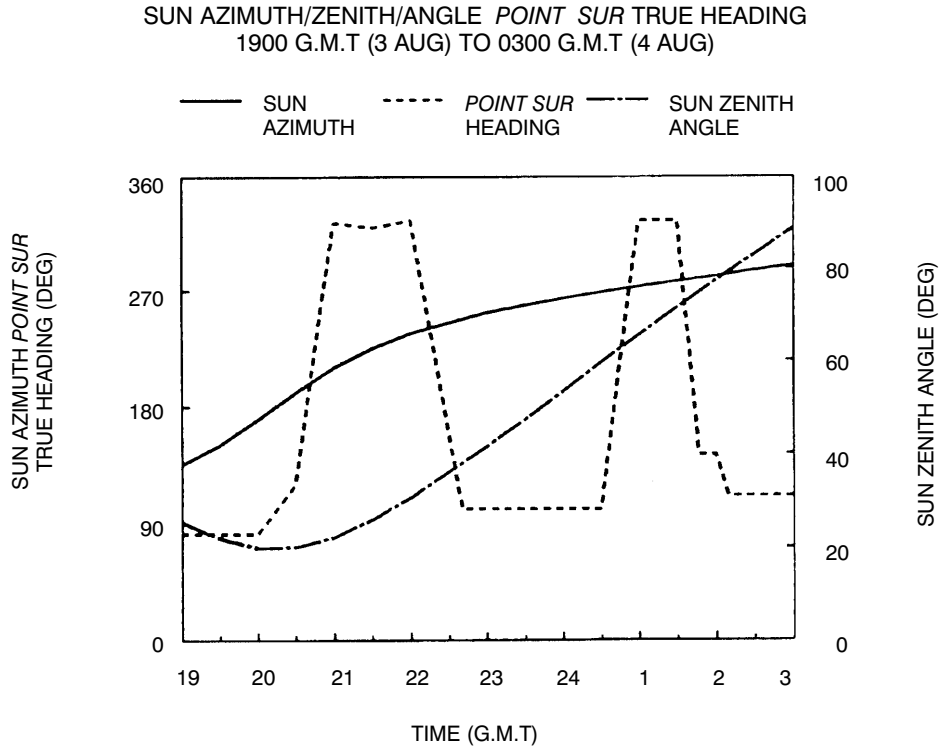

Figure 4. Heading of the R/V *Point Sur* and the sun's azimuth and zenith angle as functions of time on 3 and 4 August 1992.

Corresponding to these course changes are changes in the predicted ship temperatures. In the following figures, the calculated temperatures are presented for different viewing (depression) angles and are compared with the zero-range temperatures determined from the AGEMA

measurements. Figures 5, 7, 9, and 11 show the predicted ship temperatures calculated by the TCM2 model, and figures 6, 8, 10, and 12 show the SHIPSIG model. In figures 5 and 6, both models predicted rising temperatures when the port side of the ship was exposed to the sun. In figures 7 and 8, both models indicate decreasing temperatures on the shaded (starboard) side of the ship. The correspondence with the measured values is within two degrees, which is within the uncertainty of the measurements themselves. Figures 5 through 8 range from 1300 to 1700 hours (local time), and figures 9 through 12 range from near sunset at 1700 to 2000 hours (local time [0000 to 0300 G.M.T.]). In figure 9 it appears that the TCM2 model over-predicts the solar effect in when the sun is low in the sky. This may be the result of errors produced by the simplified three-layer transmission model employed by TCM2. The corresponding values calculated by the SHIPSIG model are shown in figure 10. The starboard calculations corresponding to the port view, figures 9 and 10, are shown in figures 11 and 12.

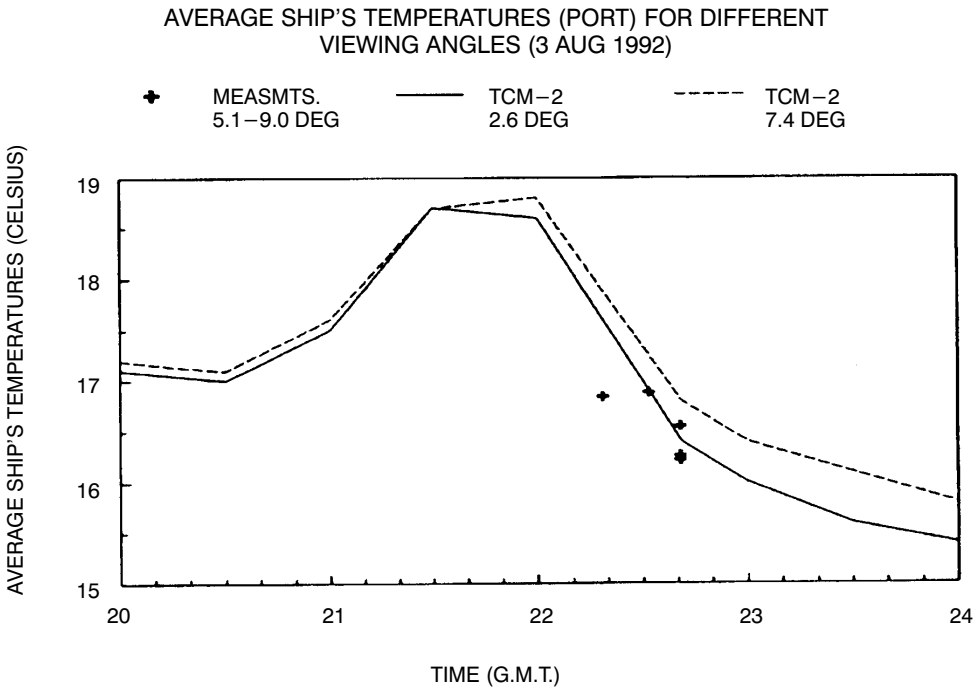

Figure 5. Comparison of measured average ship's temperatures (port side) and those calculated by TCM2 for the time period 2000 to 2400 G.M.T. on 3 August 1992 for different viewing angles.

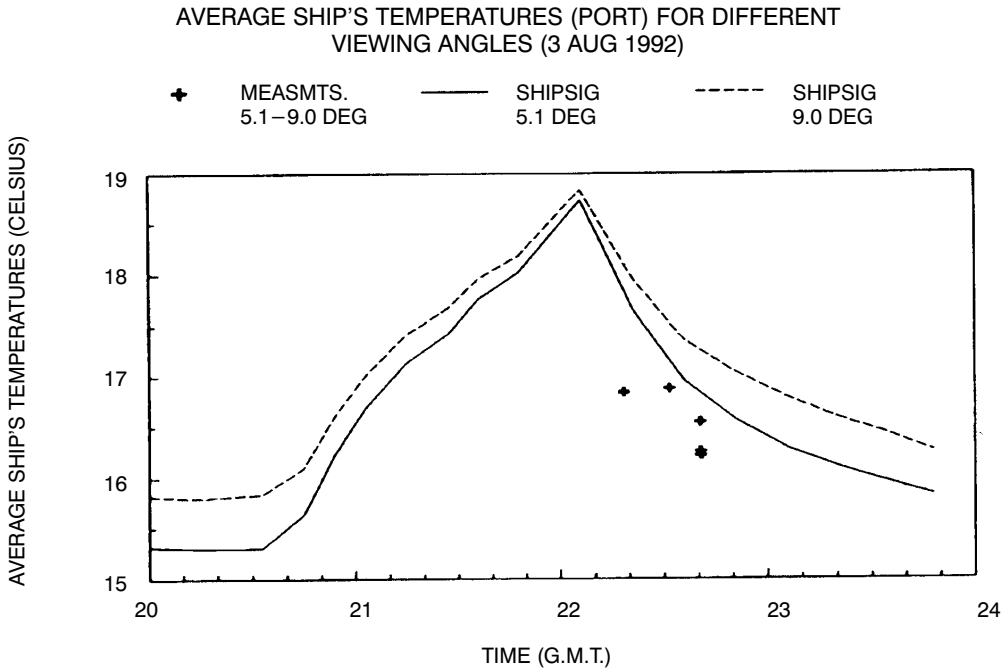

Figure 6. Comparison of measured average ship's temperatures (port side) and those calculated by SHIPSIG for the time period 2000 to 2400 G.M.T. on 3 August 1992 for different viewing angles.

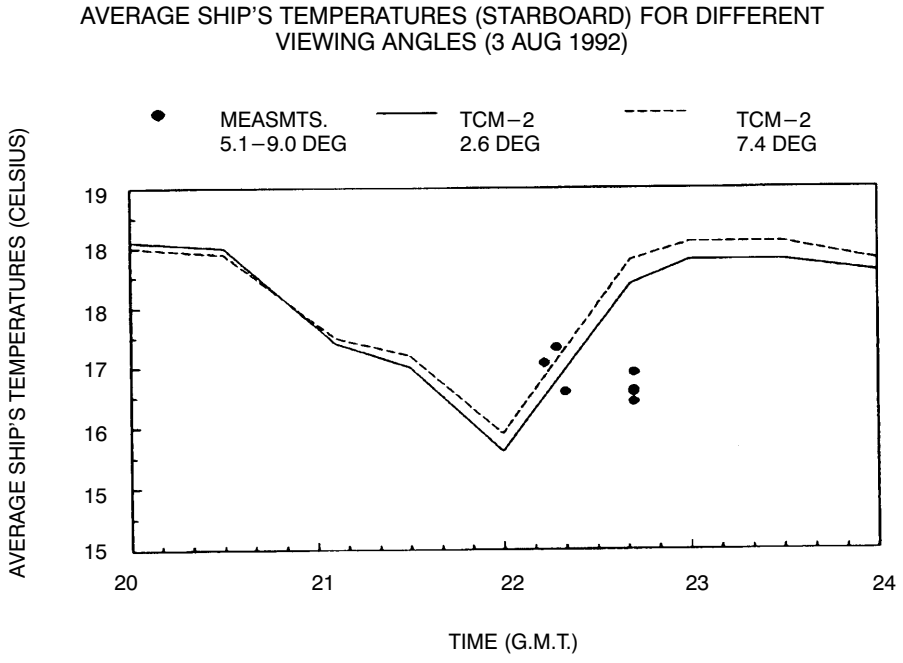

Figure 7. Comparison of measured average ship's temperatures (starboard side) and those calculated by SHIPSIG for the time period 2000 to 2400 G.M.T. on 3 August 1992 for different viewing angles.

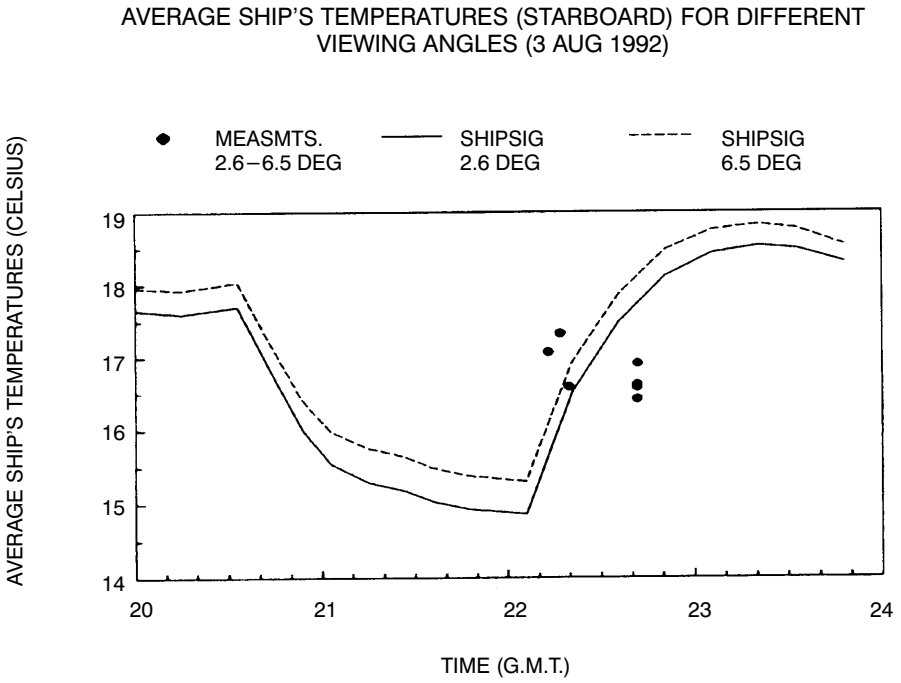

Figure 8. Comparison of measured average ship's temperatures (starboard side) and those calculated by TCM2 for the time period 2000 to 2400 G.M.T. on 3 August 1992 for different viewing angles.

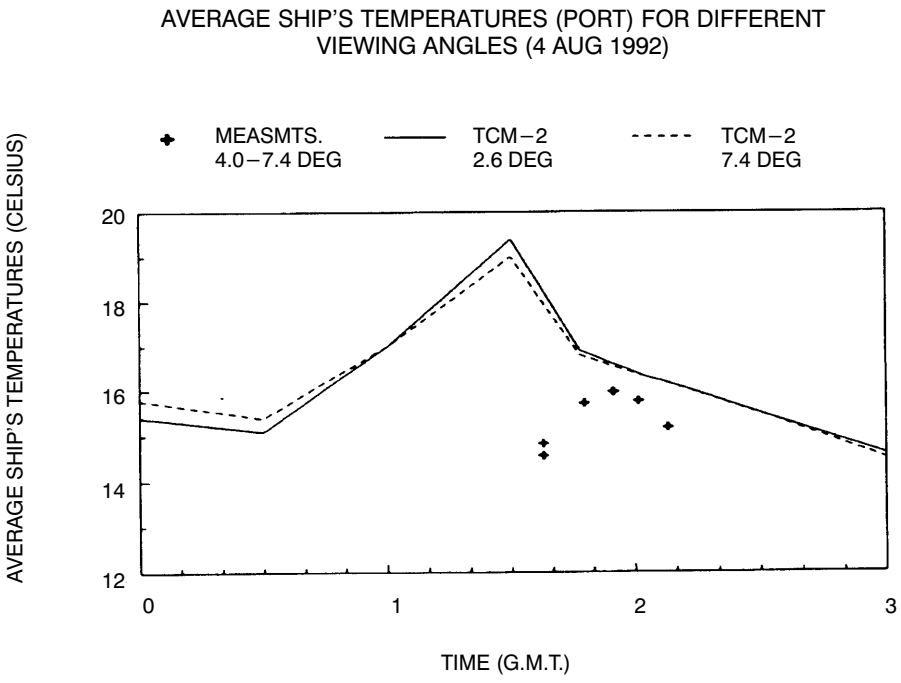

Figure 9. Comparison of measured average ship's temperatures (port side) and those calculated by TCM2 for the time period 0000 to 0300 G.M.T. on 4 August 1992 for different viewing angles.

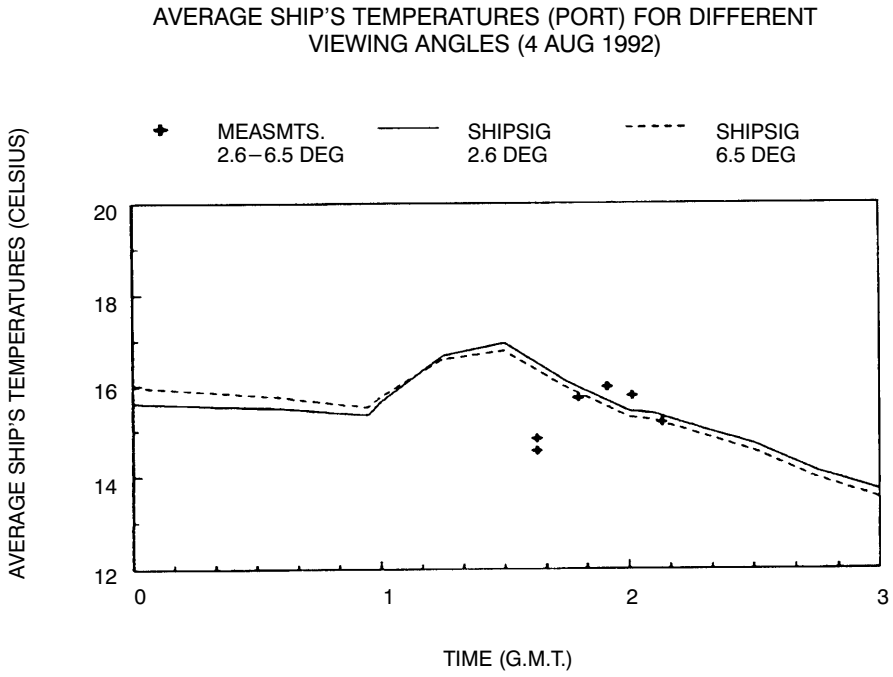

Figure 10. Comparison of measured average ship's temperatures (starboard side) and those calculated by SHIPSIG for the time period 0000 to 0300 G.M.T. on 4 August 1992 for different viewing angles.

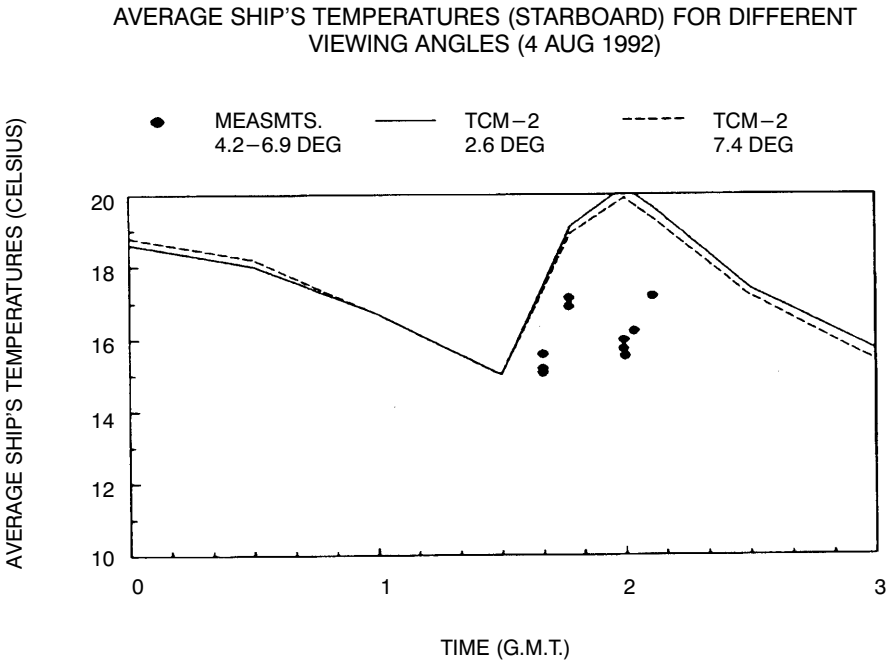

Figure 11. Comparison of measured average ship's temperatures (starboard side) and those calculated by TCM2 for the time period 0000 to 0300 G.M.T. on 4 August 1992 for different viewing angles.

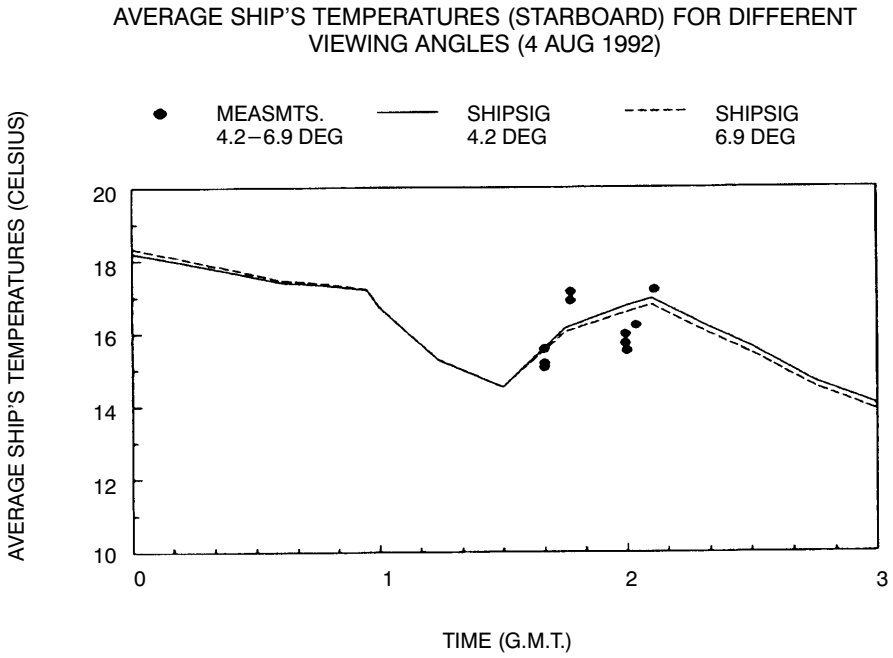

Figure 12. Comparison of measured average ship's temperatures (starboard side) and those calculated by SHIPSIG for the time period 0000 to 0300 G.M.T. on 4 August 1992 for different viewing angles.

CONCLUSIONS

The temperatures calculated by both models are insensitive to the viewing angle in figures 5 through 12. While the inputs to both the TCM2 and SHIPSIG models are the same, their signatures in figures 5, 6, 7 and 8 differ in shape, but are within one to two degrees of each other. Both of the models respond equally to the solar insolation effects during the first time period on 3 August (high solar elevation angle), and the calculated temperatures agree well (within one degree Celsius) with the measurements. For the second time period on 4 August (low solar elevation angle), the TCM2 model predicted a peak in the average port side temperature, which is greater (approximately two degrees C) than the SHIPSIG value (figures 9 and 10). After the final change to an easterly course on that day, the TCM2 model also predicted a greater solar heating effect on the starboard side (approximately two degrees C) than did the SHIPSIG model (figures 11 and 12). In these instances, the SHIPSIG model is in better agreement with the measurements; however, the TCM2 calculations were made using the one-dimensional, intermediate grade model. The apparent TCM2 over-prediction of the target temperature at low solar elevation angles may be an anomaly of this data set, or may be caused by the degraded three-layer LOWTRAN code used in the TCM2 model. The TCM2 intermediate grade was used for this report because the intermediate grade is employed in the EOTDA Mark 3 that is to be included in TESS(3). These same comparisons need to be made with the TCM2 research grade model, and more exhaustive tests need to be performed with additional data sets.

REFERENCES

Blakeslee, L., and L.J. Rodriguez. 1992. “User’s Manual for TCM2,” Georgia Institute of Technology, interim report for period July–December under Contract F33615–88–1865 (January 1993), Wright–Patterson AFB, OH.

Cox, C., and W. Munk. 1954. “Measurements of Roughness of the Sea Surface from Photographs of the Sun’s Glitter,” *Jour. Opt. Soc. of Am.*, 44: 838–850.

Freni, J.M.L., C.N. Touart, M.J. Gouveia, D.A. DeBenedictis, I.M. Halberstam, D.J. Hamann, P.F. Hilton, D.B. Hodges, D.M. Hoppes, J.J. Oberlatz, M.S. Odle, C.N. Touart, and S–L Tung. 1993. “Electro-Optical Tactical Decision Aid (EOTDA) User’s Manual, Version 3, Volume 11,” Phillips Laboratory Technical Report PL–TR–93–2002 (II).

Hughes, H.G., and C.P. McGrath. 1993. “Surface Ship Infrared Signatures Determined Using an Airborne Imaging System,” Science and Technology Corporation Technical Report 2727, September.

Kneizys, F.X., E.P. Shettle, W.O. Gallery, J.H. Chetwynd, Jr., J.H. Abreu, J.E.A. Selby, S.A. Clough, and R.W. Fenn. 1983. “Atmospheric Transmittance/Radiance: Computer Code LOWTRAN 6,” Air Force Geophysical Laboratory Technical Report No. 83–0187.

Kneizys, F.X., E.P. Shettle, L.W. Abreu, J.H. Chetwynd, Jr., G.P. Anderson, W.O. Gallery, J.E.A. Selby, and S.A. Clough. 1988. “User’s Guide to LOWTRAN 7,” Air Force Geophysical Laboratory Technical Report No. 88–0177.

Littfin, K.M. 1992. “Technical Manual, Redesigned ARC–2A Automatic Radon Counter,” NRaD Technical Report 2395 (September). San Diego, CA.

McGrath, C.P. 1992. “PREOS Program for Determining Detection Ranges of Airborne FLIR Systems,” NRaD Technical Report 1488 (January). San Diego, CA.

Ostrowski, P.P. 1993. “A Simple Thermal Model for FLIR Detection Range Applications,” meeting of IRIS Specialty Group on Targets, Backgrounds, and Discrimination, Vol II, pp 177–190 (July).

Ostrowski, P.P., and D.M. Wilson. 1985. “A Simplified Computer Code for Predicting Ship Infrared Signatures,” Naval Surface Warfare Center Technical Report 84–540.

Wollenweber, F.G. 1988. “Infrared Sea Radiance Modeling Using LOWTRAN 6,” Naval Ocean Systems Center Technical Document 1355, San Diego, CA.

Wollenweber, F.G. 1990. “Impact of Atmospheric Layering on LOWTRAN 6 Radiance Calculations,” *Appl. Opt.*, 29: 5177–5181.

GLOSSARY

ARC–2A	Automatic Radon Counter #2A
EOSPA	Electro-Optical Systems Performance Assessment
EOTDA	Electro-Optical Tactical Decision Aid
FLIR	Forward-Looking Infrared System
FOV	Field-of-view
G.M.T	Greenwich Mean Time
GPS	Global Positioning System
LOWTRAN	Low Transmission
NAM	Navy Aerosol Model
NRaD	Naval Command, Control and Ocean Surveillance Center RDT&E Division
NSWCWODET	Naval Surface Warfare Center White Oak Detachment
PREOS	Performance and Range of Electro-Optical System
SHIPSIG	Ship Signature
TCM2	Target Contract Model #2
TAMPS	Tactical Aircraft Mission Planning System
TESS	Tactical Environmental Support System

APPENDIX A

DESCRIPTION OF THE HAROLD E. HOLT VLF ANTENNA

The VLF antenna at HEH, termed a TRIDECO type of antenna (HNCD, 1967), is an electrically short top-loaded monopole, as are all the US Navy's VLF antennas. The top-load of the HEH antenna is made up of six diamond-shaped panels. These panels are formed by eight wires that run out from the antenna center and one catenary wire across these wires in the center of the diamond for support (figure A-1). An overall top view of the antenna is given in figure A-2. Note that the panels are labeled A through F when viewed clockwise from above.

The six panels are supported by 13 towers. The towers are positioned with one tower in the center known as TO. Six odd-numbered towers (Tl-Tll) are located on an outer ring with radius 4126 ft. Six more even numbered towers (T2-T12) are located on an inner ring centered on TO with radius 2124 ft. TO is 1271 ft tall, the towers on the inner ring are 1175 ft tall, and the towers on the outer ring are 996 ft tall.

The outer apex of panel A is supported by the halyard from tower Tl. The center catenary of panel A is supported between T12 and T2. Feeders are labeled with letter of the corresponding panel.

The towers, numbered clockwise, are all grounded and supported with grounded guy wires. Top-load panels are hoisted into position by 4-part halyards attached to permanent winches at the tower base. The halyards are insulated from the panel by a string of eight Lapp compression cone insulators located at the panel corners.

The transmitter and antenna tuning system are located in a building built around the base of TO. The antenna current exits this building through two feed-through bushings on the roof. The antenna current then flows in three insulated 4-wire cages, called the feed bus system, to the pulloff insulator structures located at three points on the edge of the roof.

From each pulloff structure, two 4-wire cages, called feeders, go out towards each of two panels. The 4-wire cage feeders are suspended between the roof pulloff structure and the counter weighted down-lead hinge. The down lead goes up to the panel from this hinge. The down lead consists of an 8-wire fan suspended from a triangular truss located in the top-load panel near the panel apex. The hinge is kept in position by an insulated line connected to a counter weight (figure A-3). The combination of the nearly horizontal feeder cage and the vertical fan connected at the counter-weighted hinge allows the top-load panel to move over large displacements without significantly increasing the mechanical load on the feeder cage or the fan.

The structure was designed to allow lowering the panels to perform maintenance. When a panel is lowered, the 4-wire cage is disconnected from the down lead hinge. The hinge is towed out away from TO as the panel is lowered to the ground.

Standard practice at HEH is to set the antenna conductors on steel barrels to reduce corrosion effects on the aluminum conductors. When a panel is lowered, about 2800 barrels are put in place to accommodate the panel. Approximately 1/2 day is needed to raise or lower a panel provided that the preparation work (placing the barrels, etc) has already been completed.

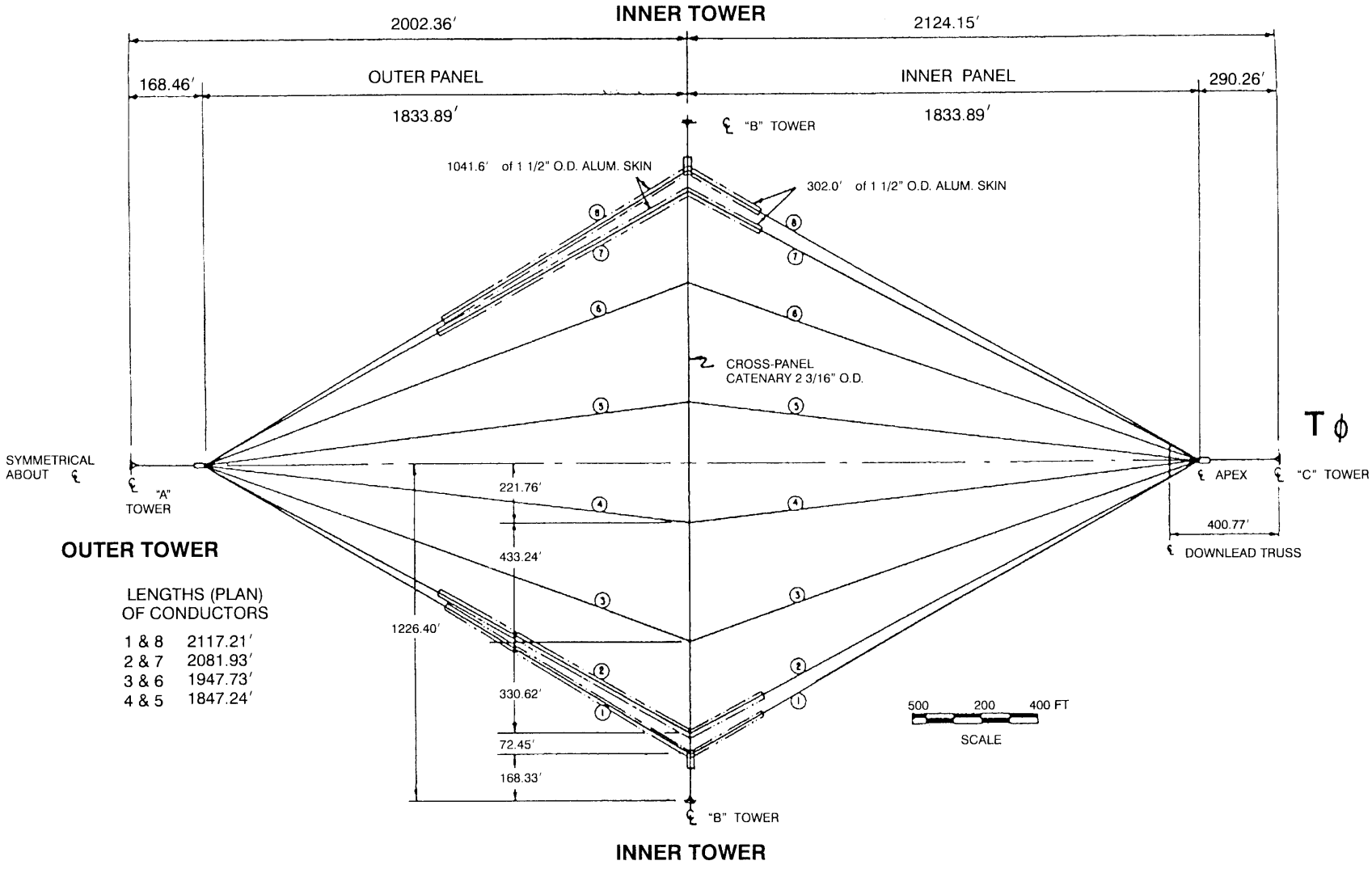

Figure A-1. Plan view of typical panel.

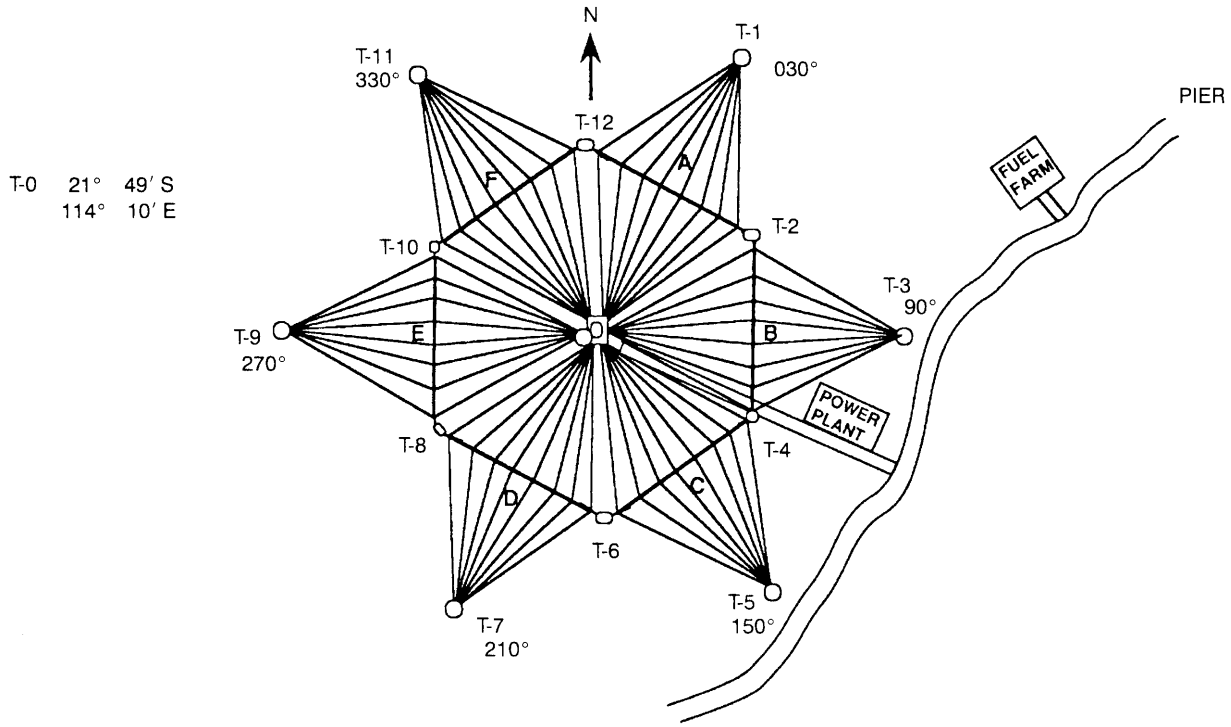

Figure A-2. Top view of VLF HEH.

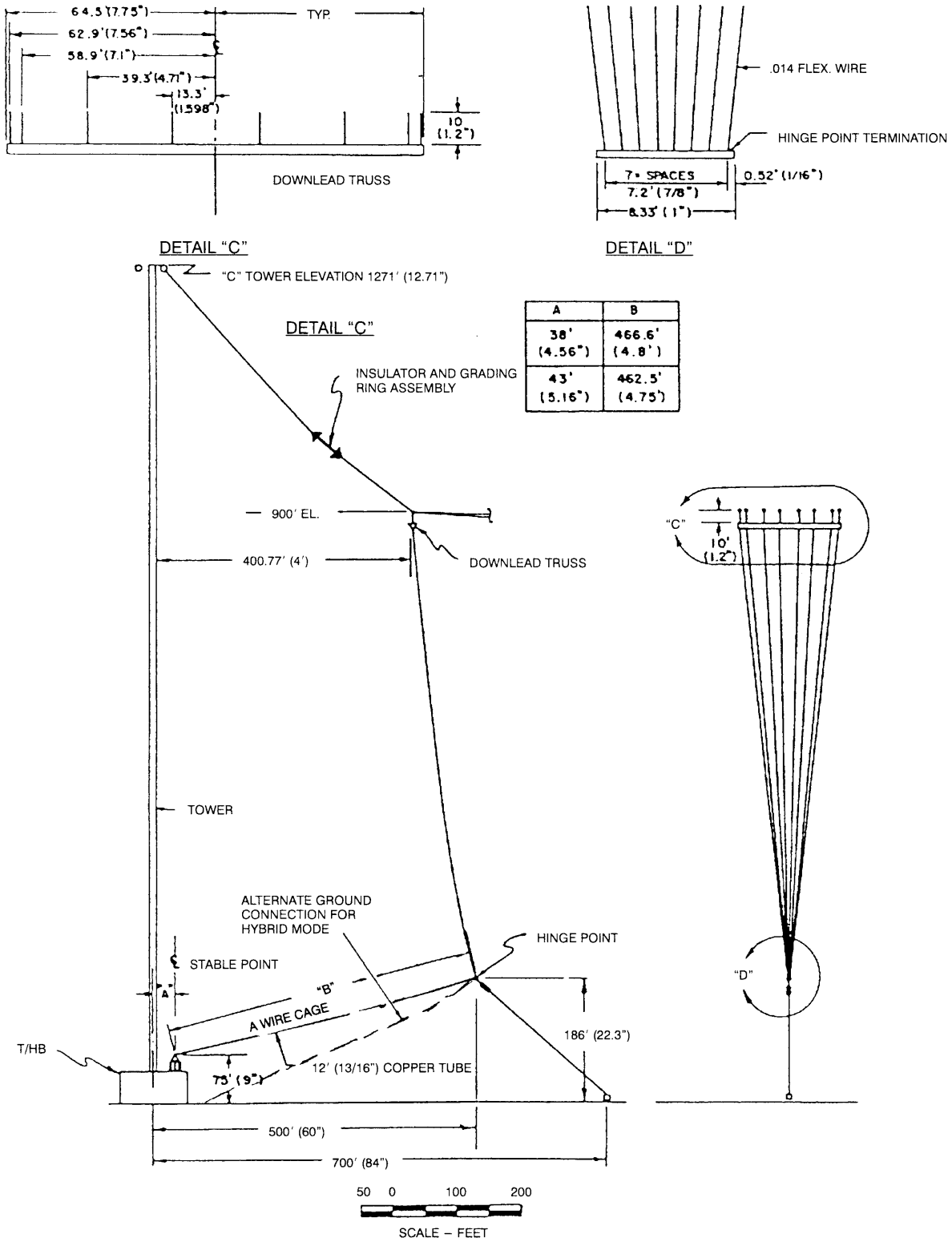

NOTE: EQIVALENT FULL-SCALE DIMENSIONS SHOWN WITH MODEL DIMENSIONS IN PARENTHESIS

Figure A-3. Antenna downlead details.

The antenna was designed to be operated with one panel lowered for maintenance. The antenna can also be operated with one or more panels deactivated by disconnecting and grounding the feed cage. This is called the hybrid mode (figure A-3). In both these conditions the antenna capacitance is reduced which means that (1) the antenna must be retuned, (2) the antenna voltages are increased, (3) the antenna bandwidth is reduced, and (4) antenna radiation efficiency is reduced slightly.

The antenna is matched and tuned by a series of switchable fixed inductors and variometers located in the helix house. The antenna impedance is converted from series to parallel resonance and transformed to a level of 9 ohms by using a coupling variometer. The parallel resonance is transformed back to series resonance and the impedance transformed to 12.5 ohms for the transmitter output by a Tee network of capacitors and inductor located in the helix house. A simplified circuit diagram is given in figure A-4. The present location of the current transformer is shown at top of the coupling coil. The loop used by NRL for the current measurement during the original proof of performance effective height measurements was located near the exit bushing. This location is also shown in the figure.

Only one panel is connected to an outer tower. The tower can be isolated by operating that panel in the hybrid mode or by lowering that panel. Two panels are connected to an inner tower. This tower can be isolated by operating both panels in hybrid mode, or by lowering one panel and operating the other in hybrid mode.

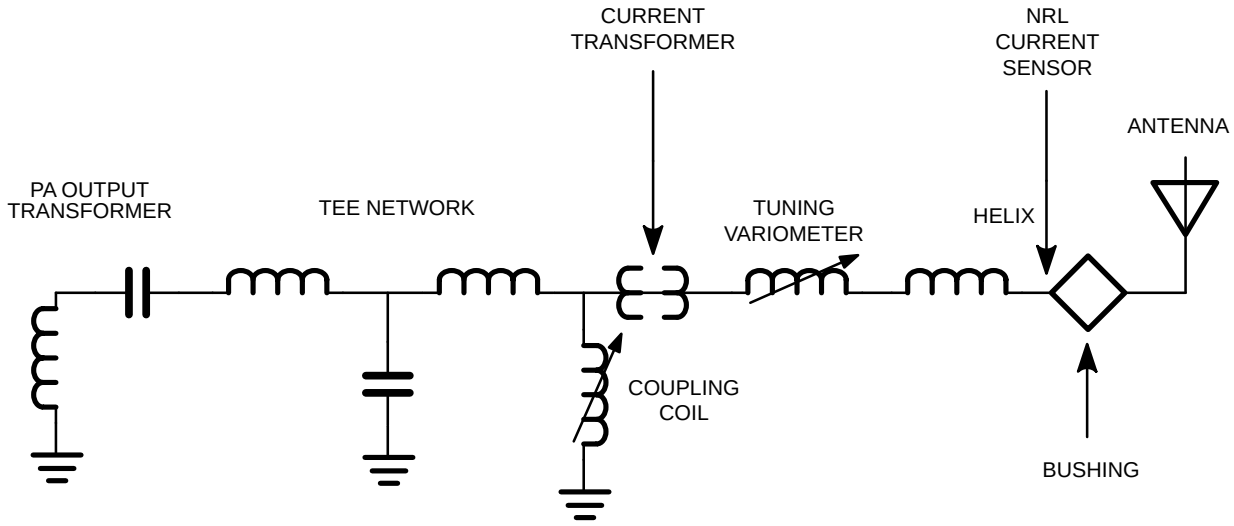

Figure A-4. VLF Holt helix house, simplified schematic diagram.

APPENDIX B

ERRORS DUE TO PERTURBATION OF MAGNETIC FIELDS

The magnetic field can be perturbed from the average value by terrain effects and local conductors such as power lines, fences, vehicles, cables, pipes, mineral deposits, etc. When selecting sites, we try to avoid as many of these objects as possible. Buried objects, since they are not visible, are particularly troublesome. The local terrain effects the magnetic field in several interesting ways. The field is typically greater than the average on the top of hills and less than average in valleys. The field can be much stronger near sharp ridges that run in a direction radial to the antenna. Near boundaries with large changes in conductivity, such as the land sea boundary, the field is often greater than average. Over the ocean, the field is stronger around the crest of sharply peaking waves, especially if the crest is in a direction approximately radial to the antenna. This appendix gives a discussion of reasons why these perturbations are considered to be random and their effects should be mitigated by averaging.

RADIATED POWER MEASUREMENT

Poynting's theorem shows that the power flowing through a closed surface is given by the integral of the Poynting vector.

$$Power = \int\int \vec{E} X \vec{H}^* \cdot d\vec{a} \quad .$$

This is the basis of the primary method for measurement of radiated power for any antenna system.

An accurate power measurement requires measurement of both *E* and *H* and phase at all points on a closed surface surrounding the antenna. This requirement can be reduced significantly by making certain assumptions.

First, far away from the antenna, there is a fixed relationship between *E* and *H*:

$$\vec{E} X \vec{H} \cdot \vec{r} = 120\pi$$

Under these conditions, *E* and *H* are perpendicular to each other and to the radius vector to the antenna. The ratio of the magnitudes of *E* to *H* is 120 π, which is the free space impedance. Because of this, radiated power can be determined by measuring the magnitude only of either *E* or *H* in the far field. If the pattern of the field is known because of theoretical considerations, it is possible to measure either *E* or *H* field at one location and infer the radiated power.

This is best illustrated by considering the example of an electrically short monopole on a perfectly conducting ground plane. Because the antenna is electrically short, it can be shown that, for fields distant from the antenna, the vertical pattern must vary as Cos(θ), where θ is the zenith angle. The azimuthal pattern must be omnidirectional. The distance required to satisfy this requirement is *r* (radius) must be much greater than both $\lambda/2\pi$ and the antenna height.

Combining the free space relationship between *E* and *H* and the Poynting's theorem gives the following equation:

$$P_r = \frac{1}{120\pi} \int \int E^2(\theta) da$$

The integration takes place over the hemisphere above the ground plane. To have a closed surface, the integral must include integration over the ground plane as well. However, since the ground is perfectly conducting, this contribution can be shown to be zero.

Adding the knowledge that the field must vary as Cos(θ), and assuming that we have made one measurement of *E* on the surface of the conducting ground (θ = 90 degrees), gives the following equation:

$$P_r = \frac{1}{120\pi} \int \int E_s{}^2(r_0)\ \mathrm{Cos}^2(\theta) da \ ,$$

where $E_s(r_0)$ is the electric field measured on the surface of the conducting ground at a distance r_0.

Using spherical coordinates (da = r^2 sin(θ) dθ dϕ) gives

$$P_r = \frac{E_s{}^2 r_0{}^2}{60} \int \sin(\theta) \cos^2(\theta)\ d\theta \ .$$

Completion of the integral gives the simple formula for radiated power

$$P_r = \frac{E_s{}^2\ (r_0) r_0{}^2}{90} \ ,$$

when MKS units are used and the field magnitudes are given in rms.

The above example illustrates how radiated power can be calculated from a single field measurement under appropriate conditions.

We next discuss application of this technique to the estimation of the power radiated from a VLF antenna. In this case, the ground is not a perfect conductor. However, at VLF, the ground conductivity usually satisfies the good conductor condition (i.e., conduction currents much greater than displacement currents). For this case, it is a very good approximation that the fields everywhere above the surface are the same as they would be if the ground were perfectly conducting at distances much less than the Sommerfeld distance. This can be seen by examination of the Sommerfeld attenuation factor (Jordan & Balmain, chapter 16). This assumption is the basis for a field strength survey in the vicinity of a few km from the antenna to be used for making the radiated power and effective height measurements.

A significant problem is that the fields measured on the surface may be perturbed locally by conducting objects, etc. The *H* field is much less perturbed than the *E* field and is, therefore, the preferred field to measure. However, the Poynting's integral still applies. Therefore, integration of the *H* field squared over a closed surface is a constant proportional to radiated power. From

this, perturbations in H^2 can be considered to be random and should average near zero for many measurements. In this case, the rms value should be the best estimate. If care is taken to use only measurements that are not greatly perturbed than the average value and rms value are essentially the same.

Measurements on the surface of the ground are not the same as measurements over the entire closed surface. However, it is clear that the expected value at a site with no perturbing influence is the same as the value that would be observed for a perfectly conducting flat earth. If the variations are small, the assumption that the perturbations average to zero is probably true, given the appropriate conditions, but I cannot formulate the conditions and prove the assumption.

Effective height is calculated at each measurement site. This calculation includes random errors in the measurement of current, distance, and magnetic field. Each of these errors is presumed to average to zero. However, rms value of field perturbation effect should average zero. The effective height formula uses each of the parameters directly (i.e., not squared). It would not be appropriate to rms value for distances and currents. This problem is alleviated by using the average field value because the field value is the same as the rms value when the perturbations are small. For this reason, it is consistent to discard all measurements three or more standard deviations from the mean.

In order for the field perturbation effect to average to zero, the measurement positions should be randomly distributed so as to not bias the measurements by a particular perturbation. For example, if the measurements were all made on the top of hills where the fields are higher than the average, the results will be biased high. Similarly, the results will be biased low if the measurements are all taken in valleys.

Our measurement procedure is to attempt to find locations where the terrain and other obvious effects are minimal.[1] We throw out measurements that deviate more than three standard deviations from the average of all the measurements. These measurements are presumed to be in error due to some hidden anomaly or some equipment problem. In this way, we reduce the measurement errors for each site. The remaining errors are assumed to be random from the argument above and averaging over many locations should reduce the power estimation error to an acceptable level.

---

[1]Sometimes this is not possible. Thus, we try to include as many of one kind of site as another. For example, at Jim Creek, the roads primarily run through the valleys. If all measurements are made in the vicinity of these roads, the resulting value for effective height will be low. Consequently, we accessed enough hilltops to round out the measurements.

APPENDIX C

CALIBRATION

NRaD maintains a special field-strength calibration facility for SPAWAR. The magnetic field-strength calibration consists of a 1-m Helmholtz coil that was constructed for NOSC by Watt Engineering. The Helmholtz coil is located in a special building constructed so as not to disturb the magnetic fields of the Helmholtz coil in the F–28 area of NRaD.

The Helmholtz coil, which is used to generate a magnetic field of known strength, consists of two single turn loops having a l m radius and spaced l m apart. The loops are connected in series to carry the same current. A precision 10-ohm resistor is connected on the ground side of the input to the Helmholtz coil to provide an accurate method of measuring current. The calibration setup is shown in figure C-l. The Helmholtz coil geometry provides the maximum volume of uniform magnetic field for a two loop system.

The NRaD Helmholtz coil system has been test calibrated by using a standard 4-turn loop. The results given in figure C-2 indicate that calibration accuracy of better than 0.025 dB can be expected up to 100 kHz.

The field in the center of the Helmholtz coil is given by

$$H = \frac{I}{\left(\frac{5}{4}\right)^{\left(\frac{3}{2}\right)} a} \quad ,$$

where a is the radius of the Helmholtz coil (l m for the NRaD coil)

The calibration procedure consists of driving the Helmholtz coil with a known current in order to generate the desired magnetic field. Placing the loop to be calibrated in the center of the Helmholtz coil and measuring the response.

The calibration data for the briefcase #3 and the blue–loop systems are given in figures C-3 through C-6. The data are given in terms of the equivalent effective height h_e'. Traditionally, the results of field strength measurements are given in terms of equivalent electric field (E') even though magnetic field is measured. The equivalent electric field is related to the magnetic field by the impedance of free space (120π ohms) . The equivalent effective height relates the meter reading to the equivalent electric field as follows.

$$120\pi H h_e' = E' h'_e = V_{loop}$$

The briefcase loop #3 system was operated in the unterminated mode at 22.8 kHz, and has an equivalent effective height of 1.83 mm (figure C–3) for large signals. It was operated in the terminated mode for the measurements on 19.8 kHz and has an equivalent effective height of 0.738 mm (figure C-4).

The blue-loop system was operated unterminated for both frequencies. The equivalent effective height for the blue loop for large signals is 2.273 mm on 22.8 kHz (figure C-5) and 1.962 mm on 19.8 kHz (figure C-6).

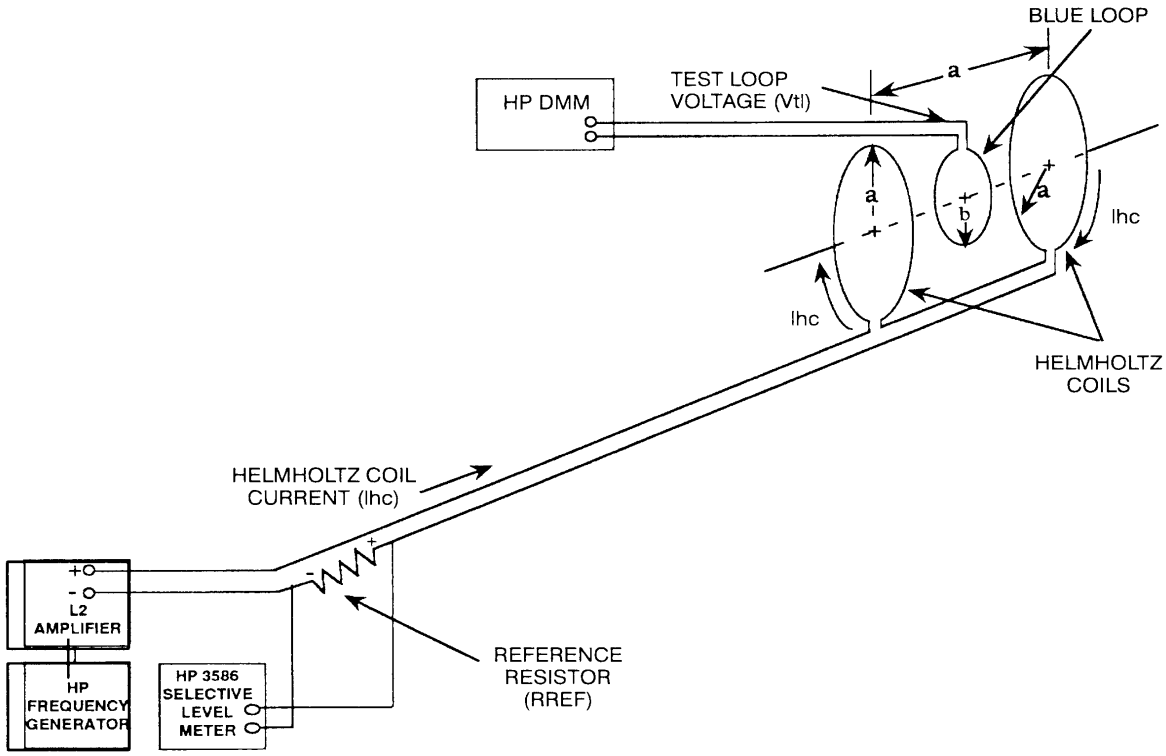

Figure C-1. H-field calibration procedure.

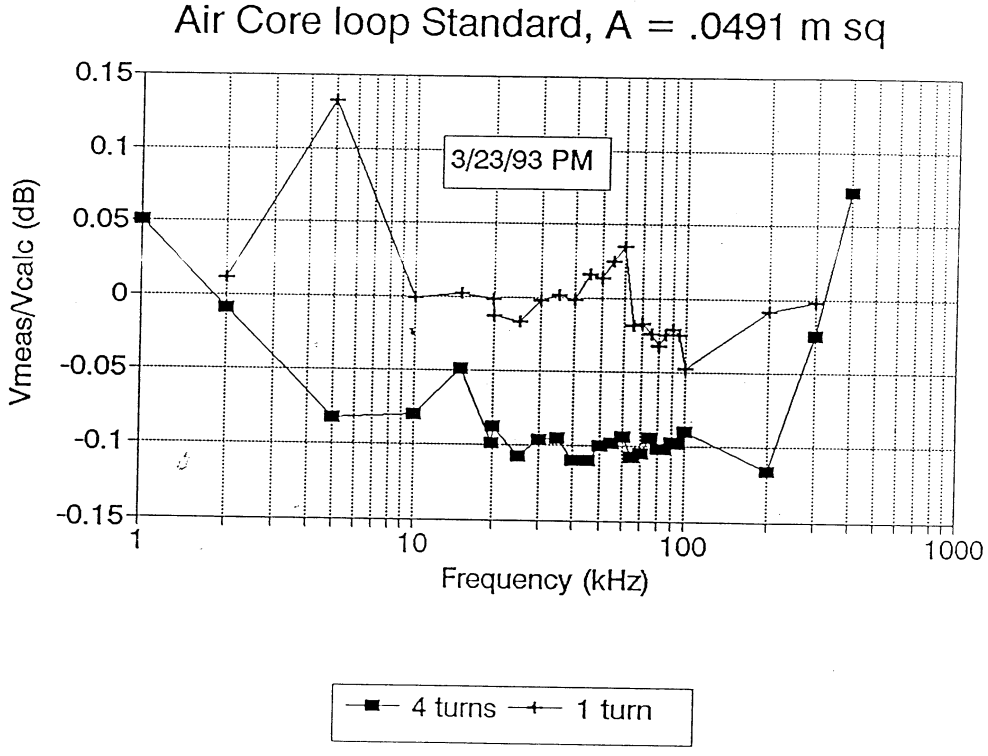

Figure C-2. NRaD 1 meter Helmholtz coil calibration.

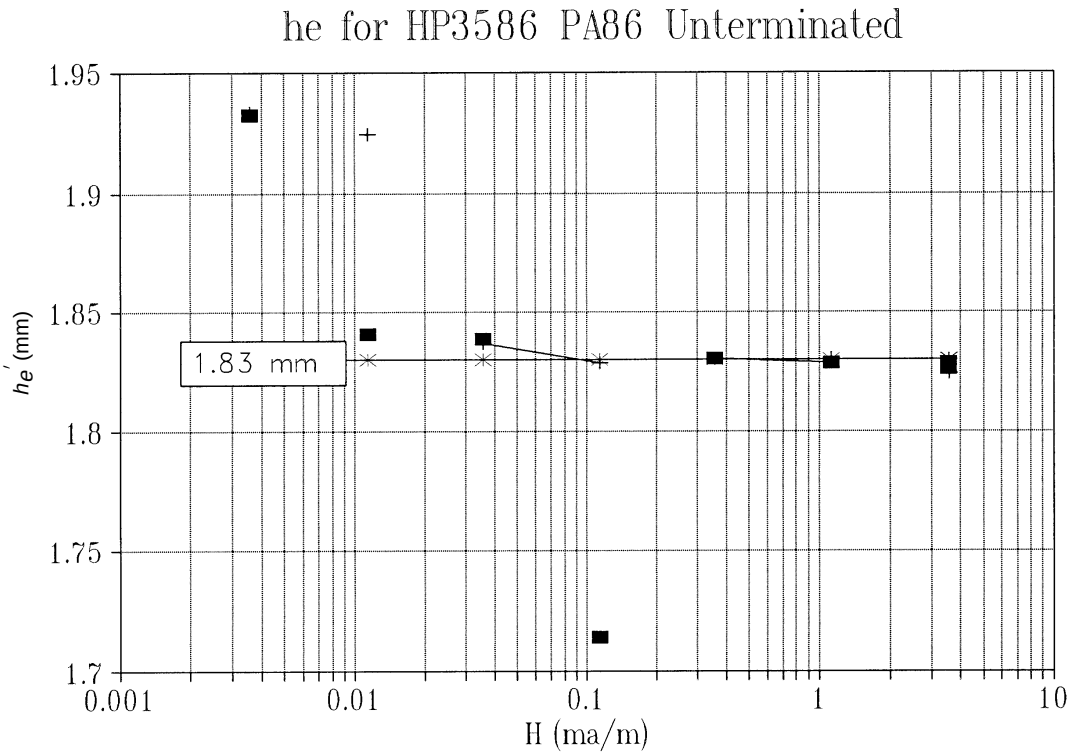

Figure C-3. Briefcase #3, calibration at 22.8 kHz, 24 June 1992.

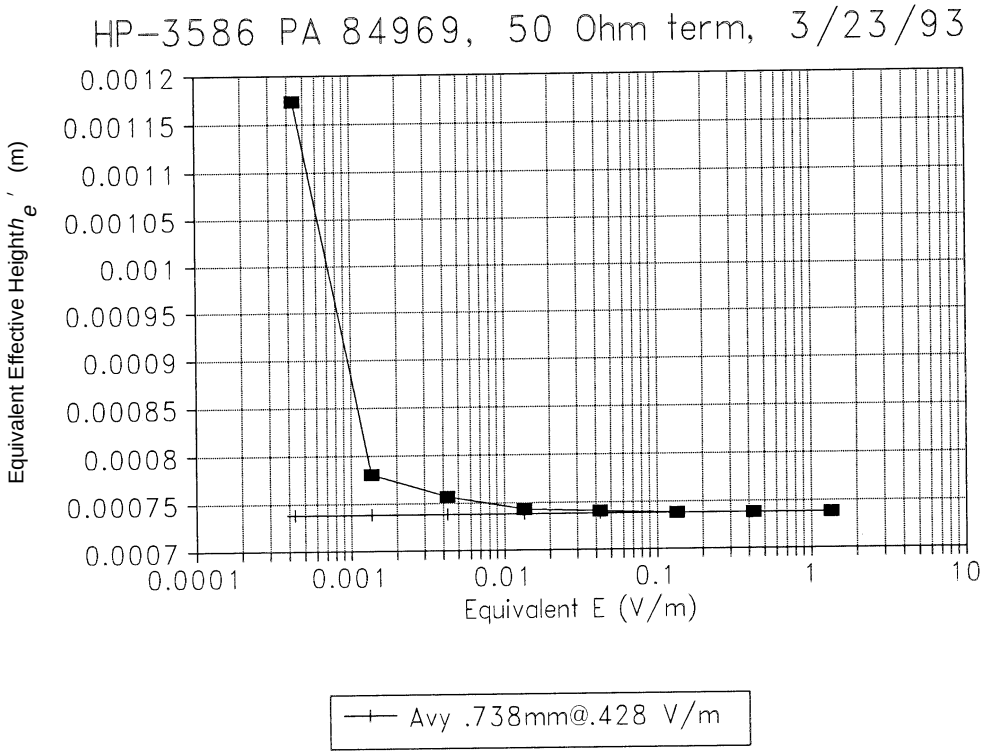

Figure C-4. Briefcase #3, calibration at 19.8 kHz.

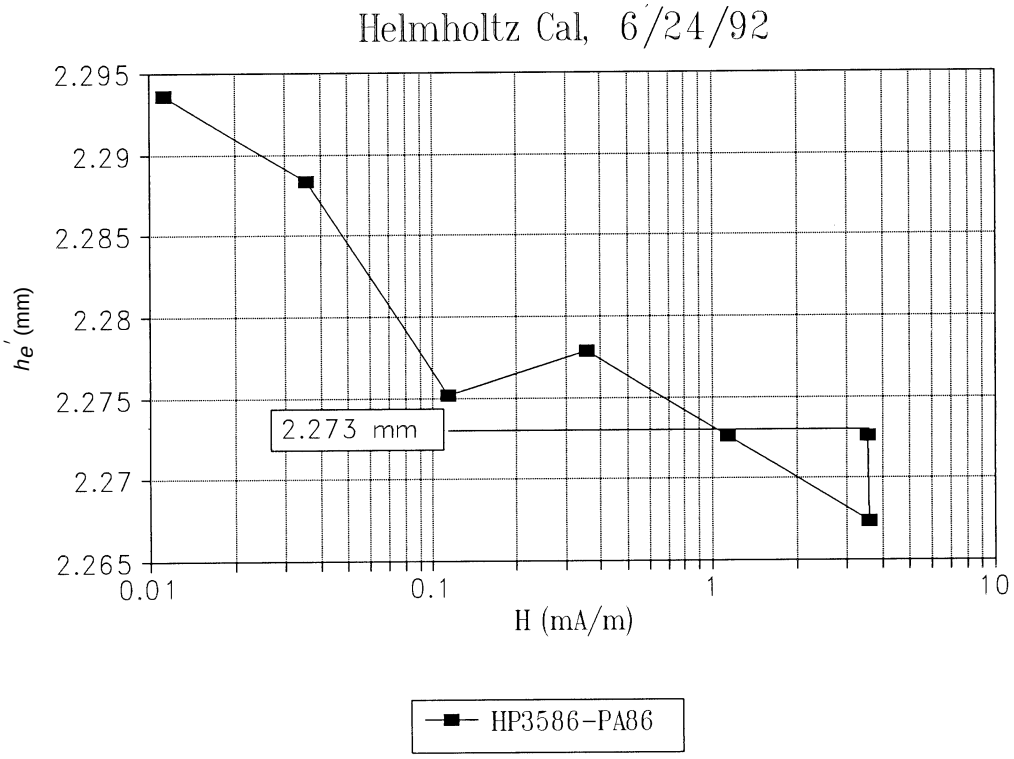

Figure C-5. Blue loop calibration, 22.8 kHz.

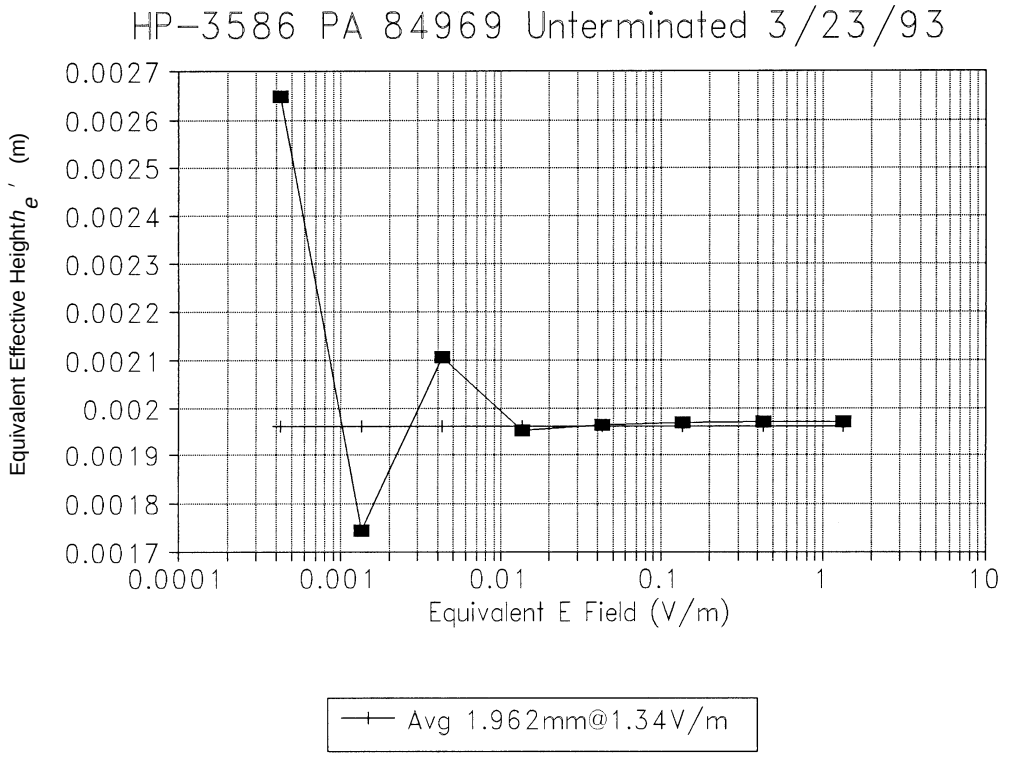

Figure C-6. Linearity check of blue loop at 19.8 kHz.

REPORT DOCUMENTATION PAGE

Form Approved
OMB No. 0704-0188

1. AGENCY USE ONLY *(Leave blank)*	2. REPORT DATE	3. REPORT TYPE AND DATES COVERED
	April 1994	Final: Aug 1992

4. TITLE AND SUBTITLE

SURFACE SHIP INFRARED SIGNATURE MODEL EVALUATION

5. FUNDING NUMBERS

PE: 0602435N
PR: RO35T84/02

6. AUTHOR(S)

C. P. McGrath, D. R. Jensen, P. P. Ostrowski

7. PERFORMING ORGANIZATION NAME(S) AND ADDRESS(ES)

Naval Command, Control and Ocean Surveillance Center (NCCOSC),
RDT&E Division
San Diego, CA 92152−5001

8. PERFORMING ORGANIZATION REPORT NUMBER

TR 1647

9. SPONSORING/MONITORING AGENCY NAME(S) AND ADDRESS(ES)

Office of Naval Research, Code 265250
800 North Quincy Street
Arlington, VA 22217

10. SPONSORING/MONITORING AGENCY REPORT NUMBER

11. SUPPLEMENTARY NOTES

12a. DISTRIBUTION/AVAILABILITY STATEMENT

Approved for public release; distribution is unlimited.

12b. DISTRIBUTION CODE

13. ABSTRACT *(Maximum 200 words)*

This report presents a case study comparison of two different models of SHIP infrared SIGnatures (SHIPSIG and TCM2) that are implemented into performance prediction codes for airborne, Forward-Looking Infrared (FLIR) systems. For this comparison, surface and vertical profile measurements of meteorological parameters were used with a modified version of the LOWTRAN 6 optical propagation code to remove the atmospheric effects on individual images of the Research Vessel *Point Sur* as recorded by an airborne AGEMA thermal imaging system. The average ship's temperatures determined at zero-range are then compared with those predicted by the two ship temperature models during clear sky conditions when the ship's heading changed to allow preferential heating of one side of the ship.

14. SUBJECT TERMS

electromagnetic
propagation
atmosphere

15. NUMBER OF PAGES

25

16. PRICE CODE

17. SECURITY CLASSIFICATION OF REPORT	18. SECURITY CLASSIFICATION OF THIS PAGE	19. SECURITY CLASSIFICATION OF ABSTRACT	20. LIMITATION OF ABSTRACT
UNCLASSIFIED	UNCLASSIFIED	UNCLASSIFIED	SAME AS REPORT